

Article

# Open-Circuit Fault Diagnosis of Wind Power Converter Using Variational Mode Decomposition, Trend Feature Analysis and Deep Belief Network

Jingxuan Zhang <sup>1,2</sup> , Hexu Sun <sup>1,3,\*</sup>, Zexian Sun <sup>2</sup>, Yan Dong <sup>1</sup> and Weichao Dong <sup>1,3</sup>

<sup>1</sup> School of Artificial Intelligence, Hebei University of Technology, Tianjin 300130, China; jingxuan.zhang@ncst.edu.cn (J.Z.); dongyan73@hebut.edu.cn (Y.D.); dongweichao@hebust.edu.cn (W.D.)

<sup>2</sup> College of Electrical Engineering, North China University of Science and Technology, Tangshan 063210, China; sunzx@ncst.edu.cn

<sup>3</sup> School of Electrical Engineering, Hebei University of Science and Technology, Shijiazhuang 050018, China

\* Correspondence: hxsun@hebust.edu.cn; Tel.: +86-1503-398-1253

Received: 25 February 2020; Accepted: 16 March 2020; Published: 21 March 2020



**Featured Application:** A novel strategy is proposed to address open-circuit fault diagnosis of grid side full-scale power converters of wind turbines.

**Abstract:** The power converter is a significant device in a wind power system. The wind turbine will be shut down and off grid immediately with the occurrence of the insulated gate bipolar transistor (IGBT) module open-circuit fault of the power converter, which will seriously impact the stability of grid and even threaten personal safety. However, in the existing diagnosis strategies for the power converter there are few single and double IGBT module open-circuit fault diagnosis methods producing negative results, including erroneous judgment, omissive judgment and low accuracy. In this paper, a novel method to diagnose the single and double IGBT modules open-circuit faults of the permanent magnet synchronous generator (PMSG) wind turbine grid-side converter (GSC) is proposed: Primarily, by collecting the three-phase current varying with a wind speed of 22 states, including a normal state and 21 failure states of PMSG wind turbine GSC as the original signal data. Afterward, the original signal data are decomposed by using variational mode decomposition (VMD) to obtain the mode coefficient series, which are analyzed by the proposed method base on fault trend feature for extracting the trend feature vectors. Finally, the trend feature vectors are utilized as the input of the deep belief network (DBN) for decision-making and obtaining the classification results. The simulation and experimental results show that the proposed method can diagnose the single and double IGBT modules open-circuit faults of GSC, and the accuracy is higher than the benchmark models.

**Keywords:** power converter; fault diagnosis; intelligent algorithm; variational mode decomposition; deep belief network

## 1. Introduction

The capacity of power converters in recent years has steadily grown in step with the increased size of large wind turbines; correspondingly, the load capacity of components of the converter have improved evidently and the electrical structure is more complex, which is bound to raise the failure rate greatly [1,2]. Meanwhile, the wind farms are mostly built in areas with abundant wind resources and complicated climate [3,4]. The operational environment of the power converter is extremely harsh, and the failure rate is high [5]. The core device of the power converter of wind turbine is the power switching component—insulated gate bipolar transistor (IGBT) module [6]. A lot of harmonics and

interharmonics will be produced if the IGBT module in a power converter has a short-circuit or open-circuit, which will impact the power quality and pollute the grid [7–10]. Then, the wind turbine would be shut down and off grid immediately, in which case seriously impacting the stability of the grid and even threatening personal safety [11]. The existing research has matured for the short-circuit fault of the power converter, and there are corresponding modules for protection [12,13]. Though there are a few achievements for the IGBT module open-circuit fault of the power converter over the years, there are few single and double IGBT modules open-circuit fault diagnosis methods producing negative results including erroneous judgment, omissive judgment and low accuracy. Moreover, due to the capability of the protection module, the short-circuit fault will turn into an open-circuit fault. Therefore, the open-circuit fault diagnosis of wind turbine power converter is crucially significant; its essence is to diagnose the power switching component, such as the IGBT module [14,15].

Over the past decade, a number of studies have been made concerning open-circuit fault diagnosis of the IGBT module in the power converter [16–21], which can be divided into qualitative fault diagnosis and quantitative fault diagnosis. Qualitative fault diagnosis includes fault tree analysis method and expert system method, whose basic idea is to build a knowledge base by using the effective experience and expertise accumulated by experts in the case of open-circuit fault of the power converter, and to determine the diagnosis results and fault causes according to certain logic reasoning for the fault status. Quantitative fault diagnosis includes the current detection method and the voltage detection method, which analyze and compare the current, voltage and other operating electrical parameters of power converter, and set thresholds when necessary, so as to make a decision and classification. The method of qualitative fault diagnosis is intuitionistic and easy to understand with clear thinking and strong logic. However, with the increasing complexity of power converter systems, the knowledge base is not comprehensive enough and the logic reasoning process is extremely complex, which makes the process of diagnosis and search difficult and the accuracy of fault diagnosis low. In order to improve the efficiency and accuracy of fault diagnosis, a combination of qualitative fault diagnosis and quantitative fault diagnosis is usually used. As stated in [22], the zero current periods are registered in each converter phase circuits. The open-circuit faults are identified calculating the average values of differences between predicted and measured phase currents. This method is insensitive to load changes but out of the high power application. [23] proposes an approach, which is based on the absolute normalized Park's current vector. This method can detect multiple open-circuit switch faults. But, this method is also prone to false alarm or failure alarm when the load changes abruptly. In [24], wavelet transform is used to preprocess load current signals, and open-circuit faults are diagnosed by the processed currents based on back propagation neural network (BPNN) and classification and regression trees (CART). As stated in [25], the fault diagnosis strategy utilizes the average values of the voltage to quickly identify failures position and devices. However, the direction of the inductor current on the primary side has to be considered first of all.

The rest of this paper is organized as follows. In Section 2, the focused topology of the GSC of PMSG wind turbine and IGBT modules open-circuit faults are addressed and analyzed. Afterward, the mathematical models of VMD, trend feature analysis method and DBN model are established and described in Section 3, respectively. Sections 4 and 5 deal with the analytical calculation of numerical simulation and experiment, some comparison results of fault diagnosis methods are shown in the end of the sections. The concluding remarks are drawn in Section 6.

## 2. Topological Graph and Fault Analysis

Up to now, the doubly fed induction generator (DFIG) and PMSG wind turbines equipped with partial scale and full scale power converters, respectively, have occupied the majority of the wind power market [26,27]. Initially, the DFIG became attractive due to the controllability of active and reactive power, having the mature technology and low cost. However, the grid code has been regularly updated, and become stricter and stricter with the steady increase of wind power penetration. Therefore, more and more wind farm operators turn to using the PMSG wind turbine equipped with

full scale power converter, due to the better low-voltage ride-through capability, higher efficiency and power density [28,29].

### 2.1. GSC Modeling

Although various power switching components can be used to match a full scale power converter, this paper only focuses on the GSC with the back to back dual pulse width modulation (PWM) structure, as it is the most used structure in the wind turbine industry. Figure 1 shows the topological graph of the GSC.

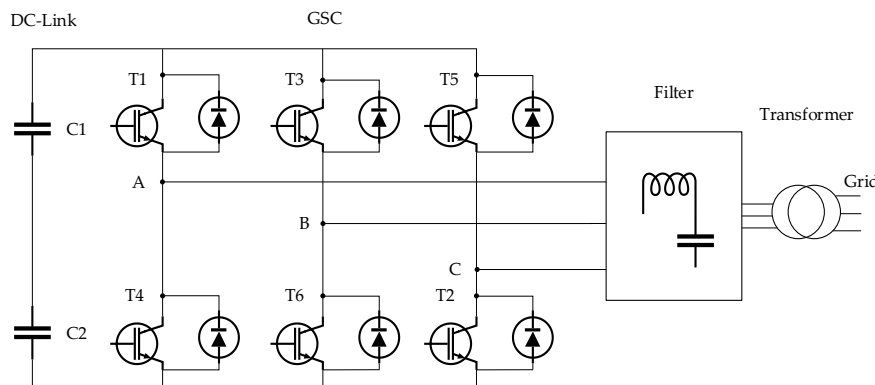


Figure 1. The topological graph of the grid-side converter (GSC).

In the Figure 1, the DC-Link is mainly consisted of shunt capacitors (C1 and C2), whose two-terminal provides a stable direct current (DC) voltage to GSC. The GSC is mainly composed of 6 IGBT modules. Every two IGBT modules compose phase A, B and C, respectively. Through PWM control strategy, the DC voltage is transformed into sinusoidal alternating current with required equivalent frequency and amplitude. Afterward, the harmonic and peak are suppressed and filtered by the filter, and the power is fed to the grid via the transformer.

For the full scale power converter of PMSG wind turbine, the key of grid connection is the GSC control strategy, which generally needs to meet two basic principles: first, to maintain the stability of DC-Link voltage. The second is to realize the control of output phase current. The relationship between the output power of the full scale converter and the wind speed can be expressed as follows:

$$P_{GSC} \approx \frac{1}{2} \rho A v^3 C_p k \tag{1}$$

where  $P_{GSC}$  is the output power of GSC,  $\rho$  is the air density in  $\text{kg/m}^3$ ,  $A$  is the sweep area of the blades in  $\text{m}^2$ ,  $v$  is the wind speed in  $\text{m/s}$ ,  $C_p$  is the power coefficient of the blade,  $k$  is the power conversion coefficient.

When the control strategy of the GSC and the load parameters are certain, the effective value of the output line voltage  $U_{AB/BC/CA}$  and the phase current  $I_{A/B/C}$  can be calculated by the DC-Link voltage:

$$U_{AB/BC/CA} = \sqrt{\frac{1}{2\pi} \int_0^{2\pi} u_{AB/BC/CA}^2 d\omega t} = 0.816 U_d, \tag{2}$$

$$I_{A/B/C} = \frac{P_{GSC}}{\sqrt{3} U_{AB/BC/CA} \cos \varphi}, \tag{3}$$

where  $u_{AB/BC/CA}$  is the output line voltage of GSC;  $U_d$  is the DC-Link voltage;  $\cos \varphi$  is power factor of a phase load. In the actual operation of wind turbine, the voltage  $U_d$ ,  $U_{AB/BC/CA}$  are constant by the function of control strategy of converter. As can be observed from (1) to (3), phase current  $I_{A/B/C}$  of GSC is nearly a cubic function of the wind speed  $v$  when the other parameters are invariant. It can be

stated that the phase current is random and unstable. Thus, it is difficult to diagnose the open-circuit fault, which is also one of the most significant differences between the wind turbine converter and other converters.

### 2.2. Faults Analysis with GSC

Most of the existing open-circuit fault diagnosis strategies of power converter are only concerning the single open-circuit failure state. However, the larger current or peak of voltage would break down another IGBT module, result in a double open-circuit faults of the IGBT modules, if the system failed to respond in time to cut off the electric energy transmission after the occurrence of single open-circuit fault. Therefore, this paper is considering the single and double IGBT modules open-circuit faults of GSC. Then, there are 21 open-circuit failure states and 1 normal operating state for the 6 IGBT models of GSC. The code of IGBT modules open-circuit fault of GSC is shown in Table 1.

**Table 1.** Code of open-circuit fault of insulated gate bipolar transistor (IGBT) modules.

Fault Type Description	T6	T5	T4	T3	T2	T1	Coding Number
Normal	0	0	0	0	0	0	1
Single open-circuit	0	0	0	0	0	1	2
	0	0	0	0	1	0	3
	0	0	0	1	0	0	4
	0	0	1	0	0	0	5
	0	1	0	0	0	0	6
	1	0	0	0	0	0	7
Double open-circuit in the same phase	0	0	1	0	0	1	8
	0	1	0	0	1	0	9
	1	0	0	1	0	0	10
Double upper open-circuit in the different phases	0	0	0	1	0	1	11
	0	1	0	0	0	1	12
	0	1	0	1	0	0	13
Double lower open-circuit in the different phases	0	0	1	0	1	0	14
	1	0	0	0	1	0	15
	1	0	1	0	0	0	16
Upper and lower open-circuit in the different phases, respectively	0	0	0	0	1	1	17
	0	0	0	1	1	0	18
	0	0	1	1	0	0	19
	0	1	1	0	0	0	20
	1	1	0	0	0	0	21
	1	0	0	0	0	1	22

Where T1, T2, T3, T4, T5 and T6 represent the corresponding IGBT modules in Figure 1. The value of  $T_i$  ( $i = 1, 2, \dots, 6$ ) are the states of IGBT modules. When the value of  $T_i$  is equal to 0, it means that  $T_i$  is operating normally at this time. When the value of  $T_i$  is equal to 1, it means that  $T_i$  is open-circuit fault at this time. The 1 to 22 are the coding number correspond to the each failure state of the IGBT modules. For instance, code 2 corresponds to 000001, which means that the T1 IGBT module is single open-circuit, other IGBT modules are normal at this time. Code 21 corresponds to 110000, which means that the T5 and T6 IGBT modules are double open-circuit, other IGBT modules are normal. According to the Table 1, technicians can clearly locate which IGBT modules in the GSC have open-circuit faults.

## 3. Fault Diagnosis Method

### 3.1. VMD Modeling

The target of VMD is to decompose a real valued input signal  $f$  into a discrete number of sub-signal  $u_k$ , that have specific sparsity properties while reproducing the input. Each mode  $u_k$  is assumed to be mostly compact around a center pulsation  $\omega_k$ , which is to be determined along with the decomposition [30,31]. A scheme to assess the bandwidth of a mode is as follows: First, for each mode  $u_k$ , compute the associated analytic signal by means of the Hilbert transform in order to

obtain a unilateral frequency spectrum. Second, for each mode, shift the mode’s frequency spectrum to “baseband”, by mixing with an exponential tuned to the respective estimated center frequency. Third, the bandwidth is now estimated through the  $H^1$  Gaussian smoothness of the demodulated signal, the squared 2-norm of the gradient. The resulting constrained variational problem is as follows:

$$\min_{\{u_k\}, \{\omega_k\}} \left\{ \sum_k \|\partial_t \left[ \left( \delta(t) + \frac{j}{\pi t} \right) u_k(t) \right] e^{-j\omega_k t} \right\|_2^2 \right\} \text{ s. t. } \sum_k u_k = f, \tag{4}$$

where  $\{u_k\} = \{ u_1, \dots, u_K \}$  is all modes.  $\{\omega_k\} = \{ \omega_1, \dots, \omega_K \}$  is center frequencies of all modes.  $K$  is the number of levels of decomposition.

In order to render the problem unconstrained, a quadratic penalty term and Lagrangian multipliers  $\lambda$  are both used. The augmented Lagrangian  $L$  is as follows:

$$L(\{u_k\}, \{\omega_k\}, \lambda) = \alpha \sum_k \|\partial_t \left[ \left( \delta(t) + \frac{j}{\pi t} \right) u_k(t) \right] e^{-j\omega_k t} \right\|_2^2 + \|f(t) - \sum_k u_k(t)\|_2^2 + \left\langle \lambda(t), f(t) - \sum_k u_k(t) \right\rangle, \tag{5}$$

Minimization  $u_k$  and  $\omega_k$ , respectively:

$$\hat{u}_k^{n+1}(\omega) = \frac{\hat{f}(\omega) - \sum_{i \neq k} \hat{u}_i(\omega) + 0.5\hat{\lambda}(\omega)}{1 + 2\alpha(\omega - \omega_k)^2}, \tag{6}$$

Which is clearly identified as a Wiener filtering of the current residual. The full spectrum of the real mode is obtained by Hermitian symmetric achievement. Conversely, the mode in time domain is procured as the real part of the inverse Fourier transform of this filtered analytic signal.

$$\omega_k^{n+1} = \frac{\int_0^\infty \omega |\hat{u}_k(\omega)|^2 d\omega}{\int_0^\infty |\hat{u}_k(\omega)|^2 d\omega}, \tag{7}$$

Which puts the new  $\omega_k$  at the center of gravity of the corresponding mode’s power spectrum. This mean carrier frequency is the frequency of a least squares linear regression to the instantaneous phase observed in the mode.

The decomposition procedure of VMD method is as follows:

Step 1. Initialize  $\{\hat{u}_k^1\}, \{\omega_k^1\}, \hat{\lambda}^1, n \leftarrow 0$ .

Step 2. Update  $u_k, \omega_k$  and  $\lambda, n \leftarrow n + 1, k = 1 : K$ .

$$\hat{u}_k^{n+1}(\omega) \leftarrow \frac{\hat{f}(\omega) - \sum_{i < k} \hat{u}_i^{n+1}(\omega) - \sum_{i > k} \hat{u}_i^n(\omega) + 0.5\hat{\lambda}^n(\omega)}{1 + 2\alpha(\omega - \omega_k^n)^2}, (\omega \geq 0), \tag{8}$$

$$\omega_k^{n+1} \leftarrow \frac{\int_0^\infty \omega |\hat{u}_k^{n+1}(\omega)|^2 d\omega}{\int_0^\infty |\hat{u}_k^{n+1}(\omega)|^2 d\omega}, \tag{9}$$

$$\hat{\lambda}^{n+1}(\omega) \leftarrow \hat{\lambda}^n(\omega) + \tau \left( \hat{f}(\omega) - \sum_k \hat{u}_k^{n+1}(\omega) \right), (\omega \geq 0), \tag{10}$$

Step 3. Repeat the iterative procedure of Step 2 until,

$$\frac{\sum_k \|\hat{u}_k^{n+1} - \hat{u}_k^n\|_2^2}{\|\hat{u}_k^n\|_2^2} < \varepsilon, \tag{11}$$

where  $\varepsilon$  is a given parameter.

### 3.2. Trend Feature Analysis of Decomposed Data

A novel method of trend feature analysis is proposed for extracting trend feature vectors in this part. The three-phase current  $I_{A/B/C}$  varying with wind speed  $v$  of GSC under 22 states are decomposed by variational mode in  $K$  levels, and each phase current gets  $K$  levels of modes:

$$A_{xu} = \{ A_{xu1}, \dots, A_{xuK} \}, \tag{12}$$

$$B_{xu} = \{ B_{xu1}, \dots, B_{xuK} \}, \tag{13}$$

$$C_{xu} = \{ C_{xu1}, \dots, C_{xuK} \}, \tag{14}$$

where  $A$ ,  $B$  and  $C$  denote the each phase of GSC in Figure 1;  $x = 1, 2, \dots, 22$  denotes fault code;  $A_{xu}$ ,  $B_{xu}$  and  $C_{xu}$  are the modes sets of three-phase current after decomposing;  $A_{xuk}$ ,  $B_{xuk}$  and  $C_{xuk}$  ( $k = 1, 2, \dots, K$ ) are the  $k$ -th mode coefficient series of three-phase current modes sets, respectively.

Extracting  $E_{Axk}$ ,  $E_{Bxk}$  and  $E_{Cxk}$  the feature energy of each mode of three-phase current can be expressed as:

$$E_{Axkj} = \sum_{j=1}^n |A_{xuk}(j)|^2, x = 1, 2, \dots, 22, k = 1, 2, \dots, K, \tag{15}$$

$$E_{Bxkj} = \sum_{j=1}^n |B_{xuk}(j)|^2, x = 1, 2, \dots, 22, k = 1, 2, \dots, K, \tag{16}$$

$$E_{Cxkj} = \sum_{j=1}^n |C_{xuk}(j)|^2, x = 1, 2, \dots, 22, k = 1, 2, \dots, K, \tag{17}$$

where  $E_{Axk}$ ,  $E_{Bxk}$  and  $E_{Cxk}$  are the feature energy of each mode of three-phase current, respectively.  $n$  is the total number of coefficients at each mode coefficient series.

The each open-circuit fault of IGBT modules would have a great impact on the feature energy in each mode of three-phase current. Therefore, the feature energy vectors  $E_A$ ,  $E_B$  and  $E_C$  could be constructed by the feature energy of each mode.

$$E_{Ax} = [ E_{Ax1} \ E_{Ax2} \ \dots \ E_{AxK} ], x = 1, 2, \dots, 22, \tag{18}$$

$$E_{Bx} = [ E_{Bx1} \ E_{Bx2} \ \dots \ E_{BxK} ], x = 1, 2, \dots, 22, \tag{19}$$

$$E_{Cx} = [ E_{Cx1} \ E_{Cx2} \ \dots \ E_{CxK} ], x = 1, 2, \dots, 22, \tag{20}$$

The three-phase current vary according to the wind speed. The same varieties occur to the feature energy of each mode. Thus, when the open-circuit happens in the GSC, the varied feature energy vectors would bring difficulties to the following data analysis. It is necessary to normalize the feature energy vectors. Let:

$$F_{Axk} = \frac{E_{Axk}}{\sum_{l=1}^K E_{Axl} + \sigma}, x = 1, 2, \dots, 22, k = 1, 2, \dots, K, \tag{21}$$

$$F_{Bxk} = \frac{E_{Bxk}}{\sum_{l=1}^K E_{Bxl} + \sigma}, x = 1, 2, \dots, 22, k = 1, 2, \dots, K, \tag{22}$$

$$F_{C_{xk}} = \frac{E_{C_{xk}}}{\sum_{l=1}^K E_{C_{xl}} + \sigma}, x = 1, 2, \dots, 22, k = 1, 2, \dots, K, \tag{23}$$

where  $\sigma$  is a tiny real number to avoid the erroneous judgment when the phase current is zero, and minimize impact on final classification results. The normalized feature energy vectors can be expressed as:

$$F_{Ax} = [ F_{Ax1} \quad F_{Ax2} \quad \dots \quad F_{AxK} ], x = 1, 2, \dots, 22, \tag{24}$$

$$F_{Bx} = [ F_{Bx1} \quad F_{Bx2} \quad \dots \quad F_{BxK} ], x = 1, 2, \dots, 22, \tag{25}$$

$$F_{Cx} = [ F_{Cx1} \quad F_{Cx2} \quad \dots \quad F_{CxK} ], x = 1, 2, \dots, 22, \tag{26}$$

Then, the factors of normalized feature energy vectors can be the function about the part factors of trend feature vectors. Let:

$$I_{x_{k=(F_{Axk})^{\frac{1}{p}}}}, x = 1, 2, \dots, 22, k = 1, 2, \dots, K, \tag{27}$$

$$I_{x_{k+K=(F_{Bxk})^{\frac{1}{p}}}}, x = 1, 2, \dots, 22, k = 1, 2, \dots, K, \tag{28}$$

$$I_{x_{k+2K=(F_{C_{xk}})^{\frac{1}{p}}}}, x = 1, 2, \dots, 22, k = 1, 2, \dots, K, \tag{29}$$

where  $p$  is a positive real number. The value of  $p$  could be confirm in an optimal range through several experiments.  $\{ I_{x_1} \quad I_{x_2} \quad \dots \quad I_{x_{3K}} \}$  is the part factors set of trend feature vectors, which could be used to judge which the phases are open-circuit. To locate the location of open-circuit IGBT module is upper or lower, 3 additional factors of trend feature vectors are needed to add in.

The first level modes of three-phase current are most similar to the original current signals. The coefficient sum of the first level modes of three-phase current can be expressed as:

$$S_{Ax1j} = \sum_{j=1}^n A_{xu1}(j), x = 1, 2, \dots, 22, \tag{30}$$

$$S_{Bx1j} = \sum_{j=1}^n B_{xu1}(j), x = 1, 2, \dots, 22, \tag{31}$$

$$S_{Cx1j} = \sum_{j=1}^n C_{xu1}(j), x = 1, 2, \dots, 22, \tag{32}$$

where  $S_{Ax1}$ ,  $S_{Bx1}$  and  $S_{Cx1}$  are the coefficient sum of the first level modes of three-phase current.  $n$  is the total number of coefficients at each mode coefficient series.

Define  $I_{x_{3K+1}}$ ,  $I_{x_{3K+2}}$  and  $I_{x_{3K+3}}$  are the 3 additional factors of trend feature vectors. Let:

$$I_{x_{3K+1}} = \begin{cases} 1 & , S_{Ax1} > 0 \\ 0 & , S_{Ax1} = 0 \\ -1 & , S_{Ax1} < 0 \end{cases}, x = 1, 2, \dots, 22, \tag{33}$$

$$I_{x_{3K+2}} = \begin{cases} 1 & , S_{Bx1} > 0 \\ 0 & , S_{Bx1} = 0 \\ -1 & , S_{Bx1} < 0 \end{cases}, x = 1, 2, \dots, 22, \tag{34}$$

$$I_{x_{3K+3}} = \begin{cases} 1 & , S_{Cx1} > 0 \\ 0 & , S_{Cx1} = 0 \\ -1 & , S_{Cx1} < 0 \end{cases}, x = 1, 2, \dots, 22, \tag{35}$$

Then, the trend feature vectors of  $x$ -th failure state is:

$$I_x = [ I_{x_1} \quad I_{x_2} \quad \dots \quad I_{x_{3K+3}} ], x = 1, 2, \dots, 22, \tag{36}$$

where  $3K + 3$  is the number of factors in each trend feature vectors.

### 3.3. DBN Modeling

In 2006, a DBN model with an efficient learning algorithm proposed by Hinton. This algorithm becomes the main framework of the deep learning algorithm later. It can extract the required features from the training set automatically [32,33]. The typical model is the restricted Boltzmann machine (RBM). The features extracted automatically solve the careless factors in the manual extraction, and initialize the weights of neural network. Then Softmax function can be used to classify, and contributes good experimental results. DBN can be composed of multi-layer RBM. A typical DBN model with double-layer RBM is shown in the Figure 2.

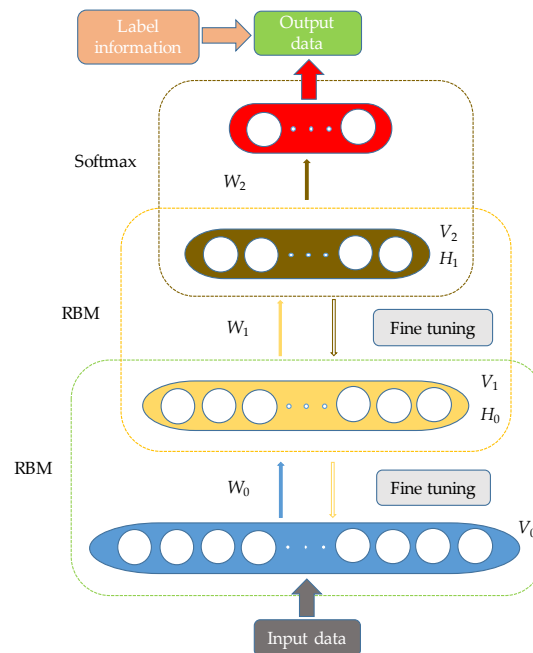


**Figure 2.** Deep belief network (DBN) model with double-layer restricted Boltzmann machine (RBM).

The process of DBN training model can be mainly divided into two steps.

Step 1: Unsupervised pretraining. Each layer of RBM network is trained independently and unsupervised to ensure that as much feature information as possible is preserved when the feature vectors are mapped to different feature spaces. The greedy method is adopted between the layers training, and the process is as follows:

1. The input layer  $V_0$  of the first RBM is also the input layer of the entire network. It typically involves training the first layer RBM by applying contrastive divergence.  $W_0$  is the weight in the first RBM.
2. The hidden layer  $H_0$  of the previous layer RBM can be seen as the visible layer  $V_1$  of the back layer RBM, followed by iterative training remaining RBM.  $W_1$  is the weight in the back layer RBM.

Step 2: Classification decision. Set the feature vectors from unsupervised reconstruction as the input feature vectors of Softmax function, which is set at the last layer of DBN to supervised train and classification decision.

### 3.4. Mission Profile of the Method

Figure 3 shows the whole process of open-circuit fault diagnosis with proposed novel method, including VMD, trend feature analysis and DBN algorithm. Above all, the three-phase current varying with wind speed of IGBT modules open-circuit of GSC are extracted under 22 states. Afterward, the three-phase current are conducted by VMD at  $K$  levels to obtain the corresponding modes. Trend feature analysis is the part proposed to address the corresponding modes data to produce the trend feature vectors under 22 states. In this part, feature energy vectors are extracted and normalized.  $3K$  factors of trend feature vectors of each state are computed with normalized data and optimal parameter  $p$ . Simultaneously, the coefficient sums of the first level modes are employed by the defined piecewise functions. The rest 3 factors of trend feature vectors of each state are obtained from the piecewise functions. Then, the trend feature vectors of each state are generated of the abovementioned factors. Finally, input the trend feature vectors to DBN, which is utilized to train, test and construct the model. The classification results output from Softmax classifier of the last layer of DBN.

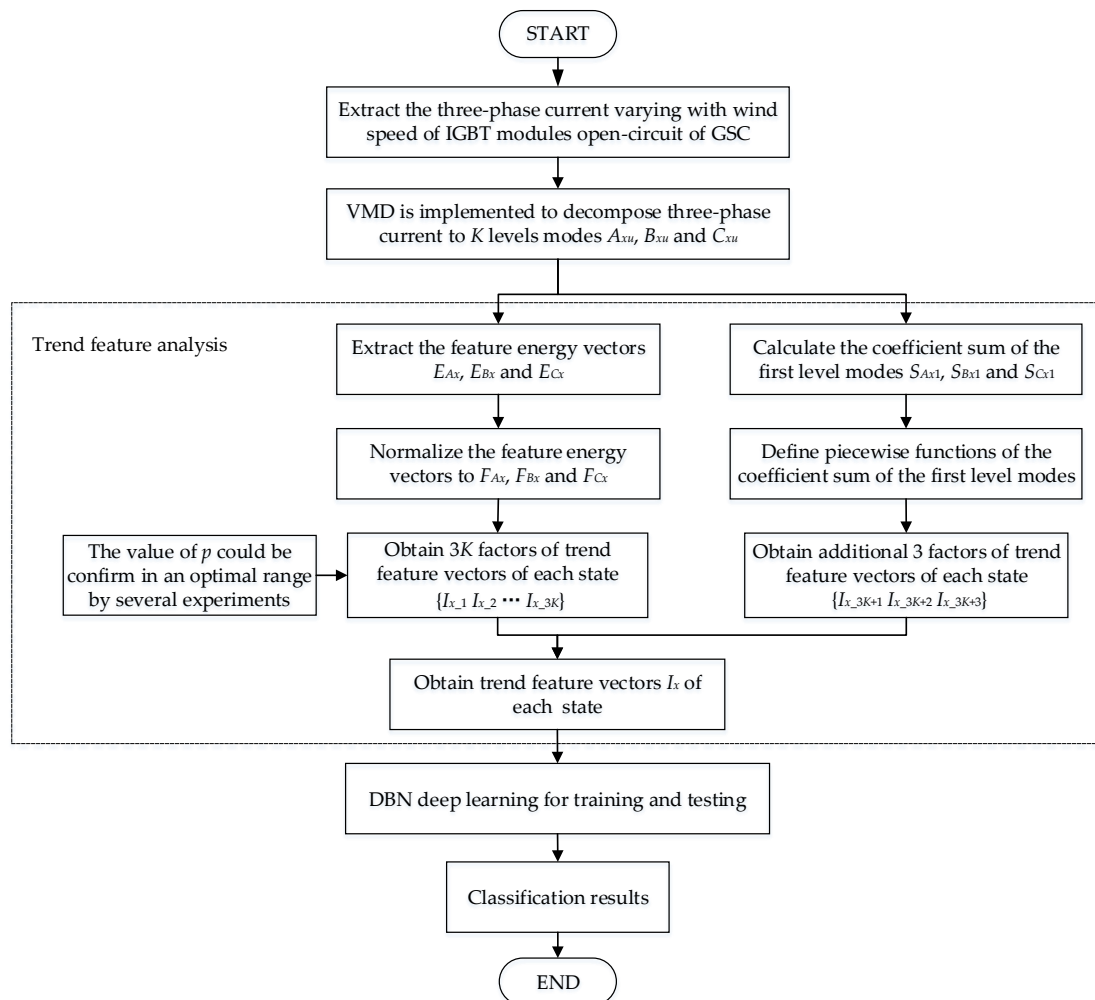


Figure 3. The mission profile of open-circuit fault diagnosis with proposed novel method.

## 4. Simulation Results

The simulation results produced from the proposed method which is addressed to diagnose the open-circuit faults of GSC are evaluated in this section.

Simulink is used to simulate 22 states of GSC of PMSG wind turbine, as shown in Figure 4. The three-phase current  $I_A$ ,  $I_B$  and  $I_C$  varying with wind speed are extracted, where the subscripts

A, B and C are the each phase. 1000 samples are extracted under each state. The length of time of each sample is between  $T$  and  $1.15T$ , where  $T$  is the period of the phase current. 800 samples out of 1000 samples under each state are randomly selected to compose training set, and the remaining 200 samples are used to compose test set. So, the sum of entire samples is 22,000, including 17,600 in training set and 4400 in test set.

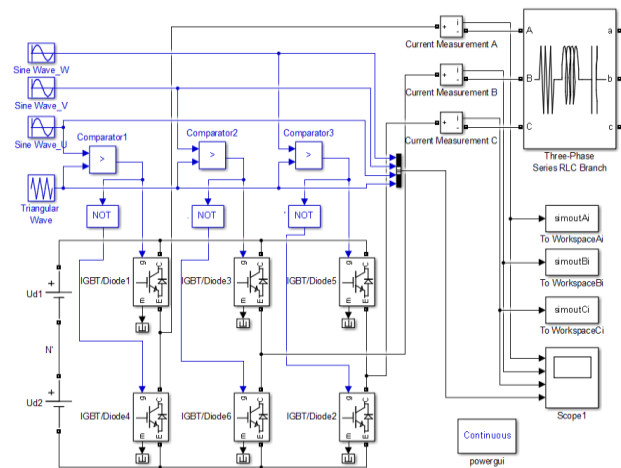


Figure 4. Simulation block diagram of GSC.

Table 2 is the parameters of main simulation components.

Table 2. Parameters of simulation components.

Item	Parameter Value
$U_d$	1050 V
$U_{AB/BC/CA}$	690 V
Voltage of sine wave	0.7 V
Frequency of sine wave	50 Hz
Frequency of triangular wave	1000 Hz
Phase difference of each phase	$120^\circ$

Where  $U_d$  denotes the voltage of DC-Link;  $U_{AB/BC/CA}$  is the line voltage of GSC; Voltage of sine wave is utilized to generate trigger signals for IGBT modules; Frequency of sine wave is equal to the rated frequency of phase current; Frequency of triangular wave is equal to the switching frequency of IGBT modules; Phase difference of each phase denotes the phase relationship between any two phases.

#### 4.1. VMD of Three-Phase Current

Considering [34], the whole three-phase current samples under 22 states are addressed by VMD at 7 levels. Figures 5 and 6 show the waveforms of three-phase current and the mode coefficient serials under No. 1 (normal operating) and No. 2 failure states, respectively. Where the red, green and blue curves denote the A, B and C phase current in Figures 5 and 6, respectively.

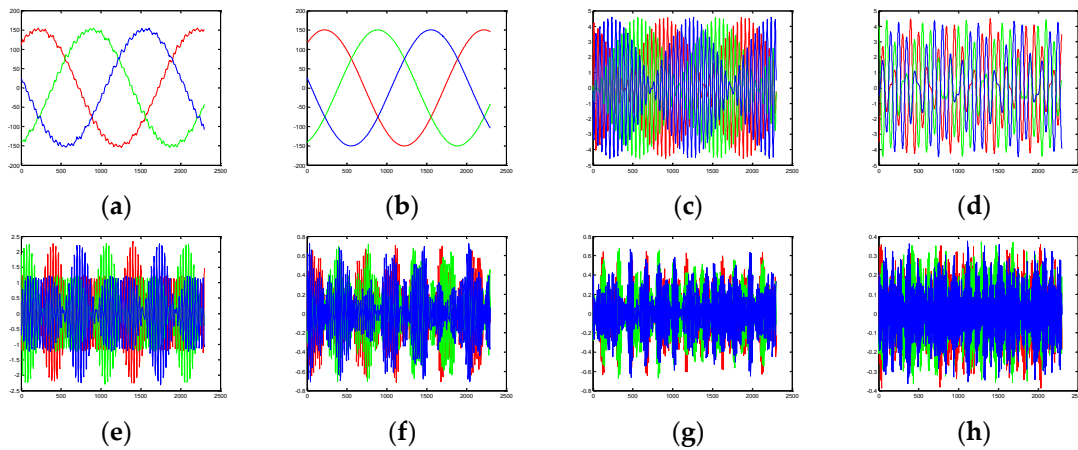


**Figure 5.** Waveforms of three-phase current and the mode coefficients serials under No. 1 state. (a) Waveform of three-phase current. (b–h) Waveforms of mode coefficients serials from 1st level to 7th level.

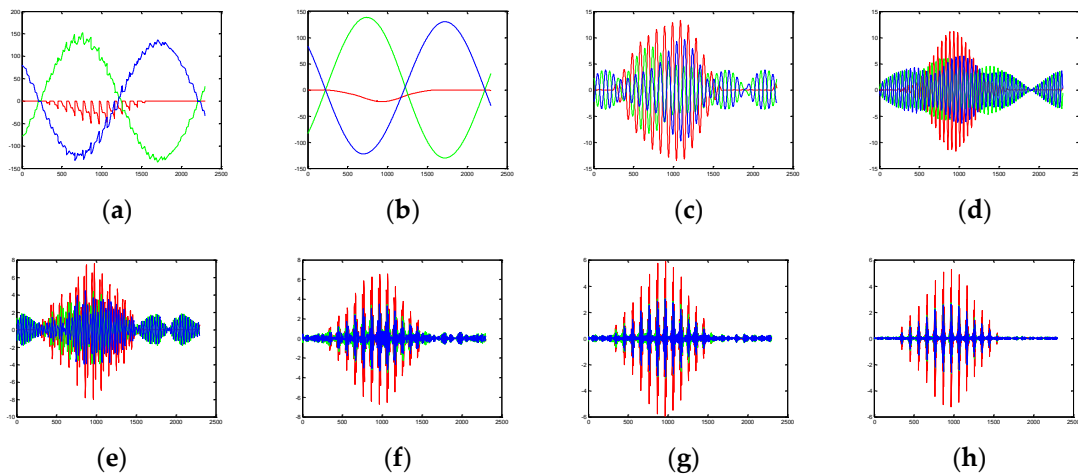


**Figure 6.** Waveforms of three-phase current and the mode coefficients serials under No. 2 failure state. (a) Waveform of three-phase current. (b–h) Waveforms of mode coefficients serials from 1st level to 7th level.

1. No. 1 state (normal operating).

It can be seen from Figure 5a that there is no phase sequence alteration, meanwhile, three-phase current is operating on a stable state. Figure 5b–h show that the waveforms of modes are relatively balanced. The feature energy of each mode decreases from the first level to seventh level. The majority feature energy is in the first level.

2. No. 2 failure state. The T1 IGBT module is open-circuit in phase-A.

It can be seen from Figure 6a that the value of phase-A current is non positive when T1 IGBT module is open-circuit. This is determined by the electrical structure and working principle of GSC. The currents of phase-B and phase-A are stable but changed in phase sequences, almost reverses for each other. Figure 6b–h show the feature energy of each level altered in phase-A modes. The proportion of feature energy of first level in phase-A is reduced. But the proportion of feature energy of other levels in phase-A are increased. The proportion of feature energy of levels of phase-B and phase-C are not sensitive to change.

### 4.2. Using Trend Feature Analysis to Extract Trend Feature Vectors

The trend feature analysis is conducted to analyze the modes coefficients serials by using (12)–(36) in Section 3. The trend feature vectors under 22 states are shown in Table 3.

**Table 3.** The trend feature vectors under 22 states of GSC.

Coding Number	1	2	3	4	...	18	19	20	21	22
$I_{x\_1}$	0.9435	0.4281	0.9139	0.8947		0.6465	0.3872	0.4256	0.6481	0.3891
$I_{x\_2}$	0.0217	0.2180	0.0312	0.0412		0.1343	0.2487	0.2414	0.1332	0.2582
$I_{x\_3}$	0.0204	0.1466	0.0268	0.0304		0.0880	0.1559	0.1426	0.0845	0.1443
$I_{x\_4}$	0.0082	0.0842	0.0121	0.0153		0.0568	0.0844	0.0735	0.0593	0.0845
$I_{x\_5}$	0.0026	0.0557	0.0074	0.0084		0.0339	0.0567	0.0533	0.0339	0.0561
$I_{x\_6}$	0.0022	0.0396	0.0050	0.0059		0.0238	0.0393	0.0369	0.0239	0.0396
$I_{x\_7}$	0.0013	0.0278	0.0034	0.0041		0.0167	0.0278	0.0266	0.0170	0.0281
$I_{x\_8}$	0.9489	0.9210	0.9099	0.4280		0.4008	0.4194	0.6516	0.3887	0.4181
$I_{x\_9}$	0.0197	0.0289	0.0339	0.2190		0.2537	0.2323	0.1291	0.2620	0.2411
$I_{x\_10}$	0.0183	0.0236	0.0270	0.1469		0.1410	0.1517	0.0893	0.1420	0.1433
$I_{x\_11}$	0.0074	0.0119	0.0135	0.0837		0.0833	0.0761	0.0559	0.0843	0.0778
$I_{x\_12}$	0.0024	0.0068	0.0072	0.0557	...	0.0551	0.0551	0.0336	0.0558	0.0544
$I_{x\_13}$	0.0020	0.0047	0.0050	0.0389		0.0386	0.0381	0.0236	0.0392	0.0383
$I_{x\_14}$	0.0012	0.0031	0.0035	0.0279		0.0276	0.0273	0.0168	0.0279	0.0270
$I_{x\_15}$	0.9478	0.9169	0.4226	0.9094		0.4116	0.6359	0.3831	0.4155	0.6470
$I_{x\_16}$	0.0198	0.0316	0.2236	0.0322		0.2471	0.1384	0.2647	0.2479	0.1327
$I_{x\_17}$	0.0185	0.0247	0.1443	0.0265		0.1424	0.0864	0.1432	0.1394	0.0868
$I_{x\_18}$	0.0083	0.0124	0.0858	0.0137		0.0788	0.0616	0.0850	0.0781	0.0581
$I_{x\_19}$	0.0023	0.0066	0.0562	0.0084		0.0549	0.0354	0.0563	0.0542	0.0342
$I_{x\_20}$	0.0021	0.0045	0.0396	0.0057		0.0382	0.0247	0.0395	0.0379	0.0241
$I_{x\_21}$	0.0012	0.0032	0.0280	0.0040		0.0271	0.0176	0.0282	0.0270	0.0170
$I_{x\_22}$	1	-1	1	-1		1	1	1	1	-1
$I_{x\_23}$	-1	-1	-1	-1		-1	-1	-1	1	1
$I_{x\_24}$	1	1	1	1		1	1	-1	-1	-1

Where the subscripts  $x$  denotes the coding number. For instance, the trend feature vectors of No. 1 state is  $I_1 = [0.9435, 0.0217, \dots, 1]$  when  $x = 1$ . The trend feature vectors of No. 21 failure is  $I_{21} = [0.6481, 0.1332, \dots, 1]$  when  $x = 21$ .

### 4.3. DBN Training and Test Results Analysis

In this paper, the input of DBN under each open-circuit failure state is a 24 dimensions trend feature vectors  $I_x = [I_{x\_1} \ I_{x\_2} \ \dots \ I_{x\_24}]$ ,  $x = 1, 2, \dots, 22$ , where  $x$  denotes the failure coding number. The DBN consists of double-layer RBM and Softmax classifier. In order to reduce the dimensions and retain the feature information of the trend feature vectors, the number of neurons in the first layer of RBM is set to 14, and the number of neurons in the second layer of RBM is set to 5. Then, the input of Softmax classifier is 5 dimensions. The output of Softmax classifier is a 22 dimensions probability vectors  $S = [S_1 \ S_2 \ \dots \ S_{22}]$ , where  $S_j (j = 1, 2, \dots, 22)$  denotes the probability of the  $j$ -th fault. Table 4 shows the probability output results of Softmax classifier and corresponding failure coding number.

Table 4 shows that, for instance, put the No. 1 trend feature vectors into DBN model, the classification result is  $S = [0.999990, 0.000000, \dots, 0.000000]$ , which means the probability of No. 1 trend feature vectors belonging to No. 1 state is 99.999%. Put the No. 22 trend feature vectors into DBN model, the classification result is  $S = [0.000000, 0.000001, \dots, 0.999997]$ , which means the probability of No. 22 trend feature vectors belonging to No. 22 state is 99.9997%. Table 4 verifies the simulation classification results generated from the proposed method are accurate to the failure coding number, if the accurate standard is upper than 50%.

**Table 4.** The probability output results of Softmax and corresponding failure coding number.

Coding Number	1	2	3	...	19	20	21	22
S <sub>1</sub>	0.999990	0.000000	0.000000		0.000000	0.000000	0.000000	0.000000
S <sub>2</sub>	0.000000	0.999999	0.000000		0.000000	0.000000	0.000000	0.000001
S <sub>3</sub>	0.000001	0.000000	0.999998		0.000000	0.000000	0.000000	0.000000
S <sub>4</sub>	0.000007	0.000000	0.000000		0.000000	0.000000	0.000000	0.000000
S <sub>5</sub>	0.000001	0.000000	0.000000		0.000000	0.000000	0.000000	0.000000
S <sub>6</sub>	0.000000	0.000000	0.000000		0.000000	0.000000	0.000000	0.000000
S <sub>7</sub>	0.000000	0.000000	0.000000		0.000000	0.000000	0.000000	0.000000
S <sub>8</sub>	0.000000	0.000000	0.000000		0.000000	0.000000	0.000000	0.000000
S <sub>9</sub>	0.000001	0.000000	0.000000		0.000000	0.000000	0.000000	0.000000
S <sub>10</sub>	0.000000	0.000000	0.000000		0.000000	0.000000	0.000000	0.000000
S <sub>11</sub>	0.000000	0.000000	0.000000		0.000000	0.000000	0.000000	0.000000
S <sub>12</sub>	0.000000	0.000000	0.000000	...	0.000000	0.000000	0.000000	0.000001
S <sub>13</sub>	0.000000	0.000000	0.000000		0.000000	0.000001	0.000000	0.000000
S <sub>14</sub>	0.000000	0.000000	0.000000		0.000003	0.000000	0.000000	0.000000
S <sub>15</sub>	0.000000	0.000000	0.000000		0.000000	0.000000	0.000000	0.000000
S <sub>16</sub>	0.000000	0.000000	0.000000		0.000000	0.000000	0.000001	0.000000
S <sub>17</sub>	0.000000	0.000000	0.000000		0.000000	0.000000	0.000000	0.000000
S <sub>18</sub>	0.000000	0.000000	0.000001		0.000000	0.000000	0.000000	0.000000
S <sub>19</sub>	0.000000	0.000000	0.000000		0.999996	0.000000	0.000000	0.000000
S <sub>20</sub>	0.000000	0.000000	0.000000		0.000000	0.999997	0.000000	0.000000
S <sub>21</sub>	0.000000	0.000000	0.000000		0.000000	0.000000	0.999998	0.000000
S <sub>22</sub>	0.000000	0.000000	0.000000		0.000000	0.000000	0.000000	0.999997

To compare the performance of proposed method, the other 7 methods are involved to address the same samples and 1 classical method stated in [16] is utilized too. The total 9 methods are: 1, proposed method, VMD, trend feature and DBN (VMD-TFA-DBN); 2, the classical method, wavelet transform, feature analysis, judgment and BPNN (WT-FA-JD-BP); 3, VMD, trend feature analysis and BPNN (VMD-TFA-BP); 4, trend feature analysis and DBN (TFA-DBN); 5, trend feature analysis and BPNN (TFA-BP); 6, VMD and DBN (VMD-DBN); 7, VMD and BPNN (VMD-BP); 8, only DBN (DBN); 9, only BPNN (BP). To increase the credibility, every method trains the same training set and tests the same test set at 100 times. Table 5 shows the comparison results between 9 methods.

**Table 5.** The simulation comparison results of open-circuit fault diagnosis under 9 methods.

Open-Circuit Fault Diagnosis Methods	Accuracy	Error Times
VMD-TFA-DBN	100%	0
WT-FA-JD-BP	99.99%	3
VMD-TFA-BP	93.26%	29,656
TFA-DBN	95.45%	20,020
TFA-BP	63.57%	160,292
VMD-DBN	20.69%	348,964
VMD-BP	16.78%	366,168
DBN	18.18%	360,008
BP	3.75%	423,500

The following conclusions can be analyzed and drawn from Table 5:

1. The method of VMD-TFA-DBN, proposed in this paper, has generated the best classifying capability under the 22 circumstances that the accuracy is 100%, the error times is 0.
2. The method of only BP has produced the worst classifying performance, the accuracy is 3.75%, the error times is 423500.
3. When the accuracy of VMD-TFA-DBN is higher than VMD-TFA-BP, TFA-DBN is higher than TFA-BP, VMD-DBN is higher than VMD-BP, and DBN is higher than BP. All of these illustrate the classification accuracy of DBN in higher than BP in the models.

4. The accuracy of each method used proposed TFA is higher than corresponding who does not use TFA, which verifies the great function of TFA for increasing classification accuracy.
5. The accuracy of each method used VMD is higher than corresponding who does not use VMD, which verifies the function of VMD in proposed method.
6. The classical method WT-FA-JD-BP has generated the second best performance that the accuracy is 99.99%, the error times is 3.

### 5. Experimental Results

In this section, experimental results are generated to verify the simulation results and analysis. As the same as simulation, the three-phase current  $I_A$ ,  $I_B$  and  $I_C$  are extracted, where the subscripts  $A$ ,  $B$  and  $C$  are the each phase. 1000 samples are extracted under each state. The length of time of each sample is between  $T$  and  $1.15T$ , where  $T$  is the period of the phase current. 800 samples out of 1000 samples under each state are randomly selected to compose training set, and the remaining 200 samples are used to compose test set. So, the sum of entire samples is 22,000, including 17,600 in training set and 4400 in test set.

Table 6 is the parameters of main components of GSC.

**Table 6.** Parameters of main components of GSC.

Item	Parameter Value
$U_d$	1050 V
$U_{AB/BC/CA}$	690 V
Voltage of sine wave	0.7 V
Frequency of sine wave	50 Hz
Frequency of triangular wave	1000 Hz
Phase difference of each phase	120°

#### 5.1. VMD of Three-Phase Current

The whole three-phase current samples under 22 states are addressed by VMD at 7 levels. Figures 7 and 8 show the waveforms of phase-A current and the mode coefficient serials under No. 1 (normal operating) and No. 2 failure states, respectively.

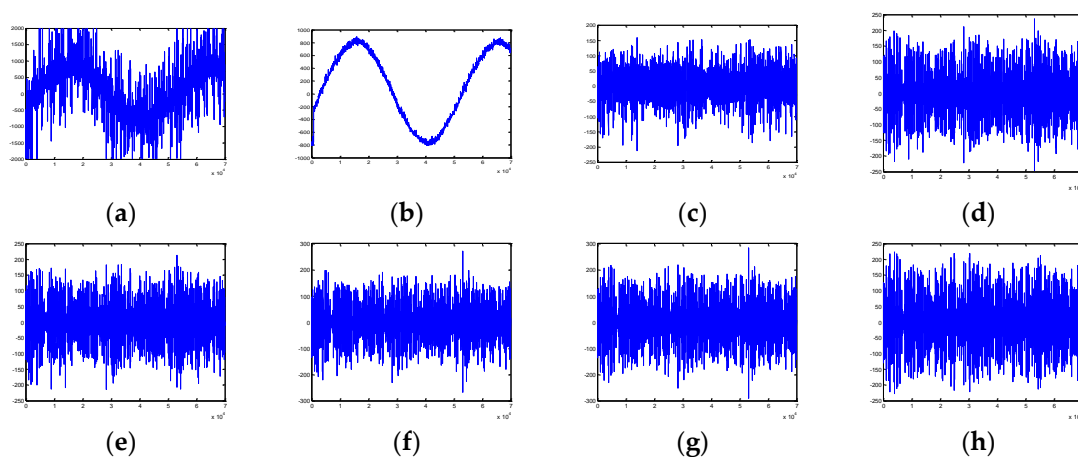


**Figure 7.** Waveforms of phase-A current and the mode coefficients serials under No. 1 state. (a) Waveform of phase-A current. (b–h) Waveforms of mode coefficients serials from 1st level to 7th level.

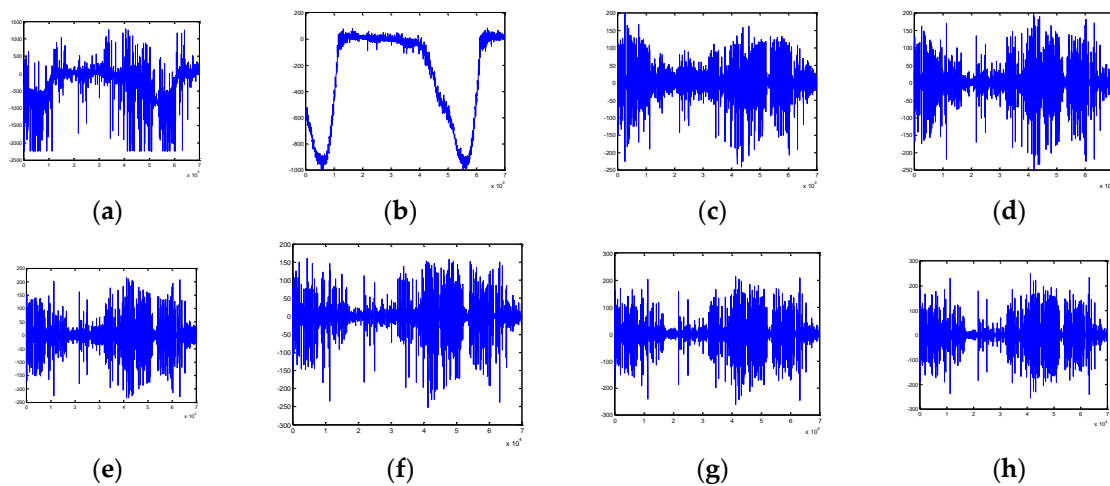


**Figure 8.** Waveforms of phase-A current and the mode coefficients serials under No. 2 failure state. (a) Waveform of phase-A current. (b–h) Waveforms of mode coefficients serials from 1st level to 7th level.

1. No. 1 state (normal operating).

It can be seen from Figure 7a that the waveforms of phase is stable as same as each phase in Figure 5a. Figure 7b–h show that the feature energy of each mode decreases from the first level to seventh level. The majority feature energy is in the first level.

2. No. 2 failure state. The T1 IGBT module is open-circuit in phase-A.

It can be seen from Figure 8a that the waveforms of phase-A is similar (to red curve) in Figure 6a. The value of phase-A current is non positive for a large majority. Figure 8b–h show the feature energy of each level altered. The proportion of feature energy of first level is reduced. But the proportion of feature energy of other levels are increased.

5.2. Using Trend Feature Analysis to Extract Trend Feature Vectors

The trend feature vectors under 22 states are shown in Table 7.

Where the subscripts  $x$  denotes the coding number. For instance, the trend feature vectors of No. 1 state is  $I_1 = [0.9434, 0.0218, \dots, 1]$  when  $x = 1$ . The trend feature vectors of No. 22 state is  $I_{22} = [0.3891, 0.2582, \dots, -1]$  when  $x = 22$ .

5.3. DBN Training and Test Results Analysis

Then, obtain the trend feature vectors  $I_x = [I_{x,1} \ I_{x,2} \ \dots \ I_{x,24}]$ ,  $x = 1, 2, \dots, 22$ , where  $x$  denotes the failure coding number. The DBN consists of double-layer RBM and Softmax classifier. The number of neurons in the first layer of RBM is set to 14, and the number of neurons in the second layer of RBM is set to 5. The output of Softmax classifier is a 22 dimensions probability vectors  $S = [S_1 \ S_2 \ \dots \ S_{22}]$ , where  $S_j (j = 1, 2, \dots, 22)$  denotes the probability of the  $j$ -th fault. Table 8 shows the probability output results of Softmax classifier and corresponding failure coding number.

Table 8 shows that, for instance, put the No. 1 trend feature vectors into DBN model, the classification result is  $S = [0.998857, 0.000000, \dots, 0.000000]$ , which means the probability of No. 1 trend feature vectors belonging to No. 1 state is 99.999%. Put the No. 22 trend feature vectors into DBN model, the classification result is  $S = [0.000000, 0.000080, \dots, 0.999353]$ , which means the probability of No. 22 trend feature vectors belonging to No. 22 state is 99.9997%. Table 8 verifies the simulation classification results generated from the proposed method are accurate to the failure coding number, if the accurate standard is upper than 50%.

**Table 7.** The trend feature vectors under 22 states of GSC.

Coding Number	1	2	3	4	...	18	19	20	21	22
<i>I<sub>x_1</sub></i>	0.9434	0.4281	0.9144	0.8946		0.6474	0.3872	0.4253	0.6489	0.3891
<i>I<sub>x_2</sub></i>	0.0218	0.2180	0.0311	0.0413		0.1342	0.2473	0.2408	0.1329	0.2582
<i>I<sub>x_3</sub></i>	0.0205	0.1466	0.0267	0.0303		0.0874	0.1558	0.1435	0.0844	0.1443
<i>I<sub>x_4</sub></i>	0.0082	0.0842	0.0121	0.0153		0.0568	0.0849	0.0739	0.0592	0.0845
<i>I<sub>x_5</sub></i>	0.0026	0.0557	0.0073	0.0085		0.0338	0.0570	0.0532	0.0338	0.0561
<i>I<sub>x_6</sub></i>	0.0022	0.0396	0.0050	0.0059		0.0238	0.0397	0.0369	0.0239	0.0396
<i>I<sub>x_7</sub></i>	0.0013	0.0278	0.0034	0.0041		0.0167	0.0281	0.0265	0.0169	0.0281
<i>I<sub>x_8</sub></i>	0.9492	0.9210	0.9103	0.4272		0.4010	0.4181	0.6511	0.3890	0.4181
<i>I<sub>x_9</sub></i>	0.0195	0.0289	0.0339	0.2199		0.2540	0.2329	0.1291	0.2620	0.2411
<i>I<sub>x_10</sub></i>	0.0183	0.0235	0.0269	0.1461		0.1403	0.1513	0.0897	0.1419	0.1433
<i>I<sub>x_11</sub></i>	0.0074	0.0119	0.0134	0.0839		0.0833	0.0765	0.0561	0.0843	0.0778
<i>I<sub>x_12</sub></i>	0.0024	0.0068	0.0071	0.0559	...	0.0551	0.0554	0.0336	0.0558	0.0544
<i>I<sub>x_13</sub></i>	0.0020	0.0047	0.0049	0.0391		0.0387	0.0383	0.0237	0.0392	0.0383
<i>I<sub>x_14</sub></i>	0.0012	0.0032	0.0035	0.0280		0.0276	0.0275	0.0168	0.0279	0.0270
<i>I<sub>x_15</sub></i>	0.9477	0.9170	0.4230	0.9092		0.4121	0.6350	0.3825	0.4164	0.6471
<i>I<sub>x_16</sub></i>	0.0199	0.0316	0.2240	0.0323		0.2471	0.1385	0.2646	0.2475	0.1328
<i>I<sub>x_17</sub></i>	0.0186	0.0247	0.1446	0.0265		0.1422	0.0865	0.1437	0.1392	0.0868
<i>I<sub>x_18</sub></i>	0.0083	0.0124	0.0854	0.0137		0.0786	0.0617	0.0852	0.0780	0.0581
<i>I<sub>x_19</sub></i>	0.0023	0.0066	0.0559	0.0084		0.0548	0.0356	0.0563	0.0541	0.0342
<i>I<sub>x_20</sub></i>	0.0021	0.0046	0.0393	0.0057		0.0381	0.0249	0.0395	0.0378	0.0241
<i>I<sub>x_21</sub></i>	0.0012	0.0032	0.0278	0.0040		0.0271	0.0178	0.0282	0.0270	0.0170
<i>I<sub>x_22</sub></i>	1	-1	1	-1		1	1	1	1	-1
<i>I<sub>x_23</sub></i>	-1	-1	-1	-1		-1	-1	-1	1	1
<i>I<sub>x_24</sub></i>	1	1	1	1		1	1	-1	-1	-1

**Table 8.** The probability output results of Softmax and corresponding failure coding number.

Coding Number	1	2	3	...	19	20	21	22
<i>S<sub>1</sub></i>	0.998857	0.000058	0.000016		0.000000	0.000000	0.000000	0.000000
<i>S<sub>2</sub></i>	0.000000	0.999602	0.000000		0.000000	0.000000	0.000000	0.000080
<i>S<sub>3</sub></i>	0.000379	0.000000	0.999668		0.000000	0.000000	0.000000	0.000000
<i>S<sub>4</sub></i>	0.000106	0.000000	0.000000		0.000059	0.000000	0.000000	0.000000
<i>S<sub>5</sub></i>	0.000130	0.000010	0.000000		0.000063	0.000060	0.000000	0.000000
<i>S<sub>6</sub></i>	0.000000	0.000000	0.000005		0.000000	0.000089	0.000060	0.000000
<i>S<sub>7</sub></i>	0.000000	0.000000	0.000000		0.000000	0.000000	0.000102	0.000044
<i>S<sub>8</sub></i>	0.000254	0.000260	0.000000		0.000000	0.000000	0.000000	0.000000
<i>S<sub>9</sub></i>	0.000183	0.000000	0.000240		0.000000	0.000000	0.000000	0.000000
<i>S<sub>10</sub></i>	0.000091	0.000000	0.000000		0.000000	0.000000	0.000000	0.000000
<i>S<sub>11</sub></i>	0.000000	0.000000	0.000000		0.000011	0.000000	0.000000	0.000000
<i>S<sub>12</sub></i>	0.000000	0.000000	0.000000	...	0.000000	0.000000	0.000000	0.000484
<i>S<sub>13</sub></i>	0.000000	0.000000	0.000000		0.000000	0.000470	0.000012	0.000000
<i>S<sub>14</sub></i>	0.000000	0.000000	0.000000		0.000713	0.000014	0.000000	0.000000
<i>S<sub>15</sub></i>	0.000000	0.000000	0.000000		0.000000	0.000000	0.000001	0.000000
<i>S<sub>16</sub></i>	0.000000	0.000000	0.000000		0.000000	0.000000	0.000285	0.000023
<i>S<sub>17</sub></i>	0.000000	0.000064	0.000002		0.000000	0.000002	0.000000	0.000000
<i>S<sub>18</sub></i>	0.000000	0.000000	0.000068		0.000001	0.000000	0.000003	0.000000
<i>S<sub>19</sub></i>	0.000000	0.000002	0.000000		0.999117	0.000000	0.000000	0.000013
<i>S<sub>20</sub></i>	0.000000	0.000000	0.000000		0.000000	0.999364	0.000000	0.000000
<i>S<sub>21</sub></i>	0.000000	0.000000	0.000000		0.000000	0.000000	0.999536	0.000003
<i>S<sub>22</sub></i>	0.000000	0.000003	0.000000		0.000036	0.000000	0.000000	0.999353

Nine compared methods mentioned in the end of Section 4 are used to compare the performance. They are involved to address the same experimental samples. To increase the credibility, every method trains the same training set and tests the same test set at 100 times. Table 9 shows the experimental comparison results between 9 methods.

**Table 9.** The experimental comparison results of open-circuit fault diagnosis under 9 methods.

Open-Circuit Fault Diagnosis Methods	Accuracy	Error Times
VMD-TFA-DBN	99.99%	3
WT-FA-JD-BP	99.99%	5
VMD-TFA-BP	91.92%	35,532
TFA-DBN	94.73%	23,178
TFA-BP	59.16%	179,714
VMD-DBN	18.25%	359,684
VMD-BP	12.42%	385,361
DBN	15.67%	371,071
BP	1.37%	433,971

The following conclusions can be analyzed and drawn from Table 9:

1. The method of VMD-TFA-DBN, proposed in this paper, has generated the best classifying capability under the 22 circumstances, with an accuracy of 99.99%, and the error times is 3.
2. The method of only BP has produced the worst classifying performance, the accuracy is 1.37%, the error times is 433971.
3. When the accuracy of VMD-TFA-DBN is higher than VMD-TFA-BP, TFA-DBN is higher than TFA-BP, VMD-DBN is higher than VMD-BP, and DBN is higher than BP. All of these illustrate the classification accuracy of DBN in higher than BP in the models.
4. The accuracy of each method used proposed TFA is higher than corresponding who does not use TFA, which verifies the great function of TFA for increasing classification accuracy.
5. The accuracy of each method used VMD is higher than corresponding who does not use VMD, which verifies the function of VMD in proposed method.
6. The classical method WT-FA-JD-BP has generated the second best performance, as the accuracy is 99.99%, and the error times is 5.

The conclusions of experimental results are broadly in line with what of simulation results. But the performance of each method of experimental results is worse than corresponding method. The probable causes are summarized as follows:

1. Three-phase current is extracted with error or interference. The samples are varying to indistinct, which lead to the accuracy decreased.
2. The total number of experimental samples in training set may be lack of, which leads to the DBN training model leaky.

## 6. Conclusions

This paper proposes a novel method to diagnosis the single and double IGBT modules open-circuit faults of GSC of the PMSG wind turbine. Above all, three-phase current varying with wind speed are extracted under 22 states. Afterward, the three-phase current are conducted by VMD at 7 levels to obtain the corresponding modes. Trend feature analysis is proposed to address the corresponding modes data to produce the trend feature vectors under 22 states. Finally, input the trend feature vectors to DBN, which is used to train and test and construct the model, and obtain the classification results.

The simulation and experimental results show that the proposed method has the capability to diagnose the single and double IGBT modules open-circuit faults of GSC, and the accuracy is high.

**Author Contributions:** J.Z. and H.S. conceived the research direction; J.Z. designed the experiments, proposed the TFA method and performed the simulation and experimental results analysis; J.Z. and Z.S. wrote the paper; Z.S., Y.D. and W.D. contributed to project research scheme formulation. All authors contributed to the final version. All authors have read and agreed to the published version of the manuscript.

**Funding:** This research was funded by the Hebei Education Department Fund (No. QN2016079), the Key Project of Hebei Natural Fund (No. E2018210044).

**Acknowledgments:** J.Z. thanks Haiyong Chen for his valuable advice. The authors thank all the reviewers and editors for their valuable comments and work.

**Conflicts of Interest:** The authors declare no conflict of interest.

## References

1. Naderi, S.B.; Davari, P.; Zhou, D.; Negnevitsky, M.; Blaabjerg, F. A review on fault current limiting devices to enhance the fault ride-through capability of the doubly-fed induction generator based wind turbine. *Appl. Sci.* **2018**, *8*, 2059. [[CrossRef](#)]
2. Tian, J.; Zhou, D.; Su, C.; Blaabjerg, F.; Chen, Z. Optimal control to increase energy production of wind farm considering wake effect and lifetime estimation. *Appl. Sci.* **2017**, *7*, 65. [[CrossRef](#)]
3. Lin, Y.G.; Tu, L.; Liu, H.W.; Li, W. Fault analysis of wind turbines in China. *Renew. Sustain. Energy Rev.* **2016**, *55*, 482–490. [[CrossRef](#)]
4. Shamsirband, S.; Rabczuk, T.; Chau, K.-W. A survey of deep learning techniques: Application in wind and solar energy resources. *IEEE Access* **2019**, *7*, 164650–164666. [[CrossRef](#)]
5. Sun, Z.X.; Sun, H.X. Health status assessment for wind turbine with recurrent neural networks. *Mathematical Probl. Eng.* **2018**, 6972481, 1–16. [[CrossRef](#)]
6. Bento, F.; Cardoso, A.J.M. A comprehensive survey on fault diagnosis and fault tolerance of DC-DC converters. *Chin. J. Electr. Eng.* **2018**, *4*, 1–12.
7. Lu, B.; Sharma, S.K. A literature review of IGBT fault diagnostic and protection method for power inverters. *IEEE Trans. Ind. Appl.* **2009**, *45*, 1770–1777.
8. Wang, H.; Zhang, C.; Zhang, N.; Chen, Y.; Chen, Y. Fault Diagnosis for IGBTs Open-Circuit Faults in High-Speed Trains Based on Convolutional Neural Network. In Proceedings of the 2019 Prognostics and System Health Management Conference, Qingdao, China, 25–27 October 2019.
9. Li, B.; Shi, S.; Wang, B.; Wang, G.; Wang, W.; Xu, D. Fault diagnosis and tolerant control of single IGBT open-circuit failure in modular multilevel converters. *IEEE Trans. Power Electron.* **2016**, *31*, 3165–3176. [[CrossRef](#)]
10. Freire, N.M.A.; Estima, J.O.; Marques, C.A.J. Open-circuit fault diagnosis in PMSG drives for wind turbine applications. *IEEE Trans. Ind. Electron.* **2013**, *60*, 3957–3967. [[CrossRef](#)]
11. Persio, D.L.; Honchar, O. Analysis of recurrent neural networks for short-term energy load forecasting. *AIP Conf. Proc.* **2017**, 1906, 190006.
12. Kuraku, N.V.P.; He, Y.; Ali, M. Fault diagnosis of open circuit multiple IGBT's using PPCA-SVM in single phase five-level voltage controlled H-bridge MLI. *IEEJ J. Ind. Appl.* **2020**, *9*, 61–72. [[CrossRef](#)]
13. Rothenhagen, K.; Fuchs, F.W. Performance of diagnosis methods for IGBT open circuit faults in voltage source active rectifiers. *IEEE Annu. Power Electron. Spec. Conf.* **2004**, *6*, 4348–4354.
14. Estima, J.O.; Cardoso, A.J.M. A new approach for real-time multiple open-circuit fault diagnosis in voltage-source inverters. *IEEE Trans. Ind. Appl.* **2011**, *47*, 2487–2494. [[CrossRef](#)]
15. Islam, F.R.; Prakash, K.; Mamun, K.A.; Lallu, A.; Pota, H.R. Aromatic network: A novel structure for power distribution system. *IEEE Access* **2017**, *5*, 25236–25257. [[CrossRef](#)]
16. Zhang, J.X.; Sun, H.X.; Sun, Z.X.; Dong, W.C.; Dong, Y. Fault diagnosis of wind turbine power converter considering wavelet transform, feature analysis, judgment and BP neural network. *IEEE Access* **2019**, *7*, 179799–179809. [[CrossRef](#)]
17. Potamianos, P.G.; Mitronikas, E.D.; Safacas, A.D. Open-circuit fault diagnosis for matrix converter drives and remedial operation using carrier-based modulation methods. *IEEE Trans. Ind. Electron.* **2014**, *61*, 531–545. [[CrossRef](#)]
18. Gan, C.; Wu, J.H.; Yang, S.Y.; Hu, Y.H.; Cao, W.P.; Si, J.K. Fault diagnosis scheme for open-circuit faults in switched reluctance motor drives using fast Fourier transform algorithm with bus current detection. *IET Power Electron* **2016**, *9*, 20–30. [[CrossRef](#)]
19. Tian, L.S.; Wu, F.; Zhao, J. Current kernel density estimation based transistor open-circuit fault diagnosis in two-level three phase rectifier. *Electron. Lett.* **2016**, *52*, 1795–1797. [[CrossRef](#)]
20. Wang, K.; Tang, Y.; Zhang, C.J. Open-circuit fault diagnosis and tolerance strategy applied to four-wire T-type converter systems. *IEEE Trans. Power Electron.* **2019**, *34*, 5764–5778. [[CrossRef](#)]

21. Li, C.; Liu, Z.; Zhang, Y.; Chai, L.; Xu, B. Diagnosis and location of the open-circuit fault in modular multilevel converters: An improved machine learning method. *Neurocomputing* **2019**, *331*, 58–66. [[CrossRef](#)]
22. Sobanski, P.; Kaminski, M. Application of artificial neural networks for transistor open-circuit fault diagnosis in three-phase rectifiers. *IET Power Electron.* **2019**, *12*, 2189–2200. [[CrossRef](#)]
23. Zhao, H.S.; Cheng, L.L. Open-circuit faults diagnosis in back-to-back converters of DF wind turbine. *IET Renew. Power Gener.* **2017**, *11*, 417–424. [[CrossRef](#)]
24. Wang, M.; Zhao, J.; Wu, F.; Yang, H. Transistor open-circuit fault diagnosis of three phase voltage-source inverter fed induction motor based on information fusion. In Proceedings of the 2017 12th IEEE Conference on Industrial Electronics and Applications (ICIEA), Siem Reap, Cambodia, 18–20 June 2017; pp. 1591–1594.
25. Zheng, M.; Wen, H.; Shi, H.; Hu, Y.; Yang, Y.; Wang, Y. Open-circuit fault diagnosis of dual active bridge DC-DC converter with extended-phase-shift control. *IEEE Access* **2017**, *7*, 23752–23765. [[CrossRef](#)]
26. Wind Power Capacity Worldwide Reaches 597 GW, 50,1 GW added in 2018 World Wind Energy Association. Available online: <https://wwindea.org/blog/2019/02/25/wind-power-capacity-worldwide-reaches-600-gw-539-gw-dded-in-2018/> (accessed on 25 February 2019).
27. Report on China's Wind Power Lifting Capacity in 2018 Chinese Wind Energy Association. Available online: [http://www.cwea.org.cn/news\\_lastest\\_detail.html?id=217](http://www.cwea.org.cn/news_lastest_detail.html?id=217) (accessed on 5 April 2019).
28. Yaramasu, V.; Dekka, A.; Duran, J.; Kouro, S.; Wu, B. PMSG-based wind energy conversion systems: Survey on power converters and control. *IET Electr. Power Appl.* **2017**, *11*, 856–968. [[CrossRef](#)]
29. Qiu, Y.; Jiang, H.; Feng, Y.; Cao, M.; Zhao, Y.; Li, D. A new fault diagnosis algorithm for PMSG wind turbine power converters under variable wind speed conditions. *Energies* **2016**, *9*, 548. [[CrossRef](#)]
30. Dragomiretskiy, K.; Zosso, D. Variational mode decomposition. *IEEE Trans. Signal Process.* **2014**, *62*, 531–544. [[CrossRef](#)]
31. Isham, M.F.; Leong, M.S.; Lim, M.H.; Ahmad, Z.A. Variational mode decomposition: Mode determination method for rotating machinery diagnosis. *J. Vibroengineering* **2018**, *20*, 2604–2621. [[CrossRef](#)]
32. Dai, J.; Song, H.; Sheng, G.; Jiang, X. Cleaning method for status monitoring data of power equipment based on stacked denoising autoencoders. *IEEE Access* **2017**, *5*, 22863–22870. [[CrossRef](#)]
33. Ma, M.; Sun, C.; Chen, X. Discriminative deep belief networks with ant colony optimization for health status assessment of machine. *IEEE Trans. Instrum. Meas.* **2017**, *66*, 3115–3125. [[CrossRef](#)]
34. Sun, Z.X.; Zhao, S.S.; Zhang, J.X. Term wind power forecasting on multiple scales using VMD decomposition, K-means clustering and LSTM principal computing. *IEEE Access* **2019**, *7*, 166917–166929. [[CrossRef](#)]



© 2020 by the authors. Licensee MDPI, Basel, Switzerland. This article is an open access article distributed under the terms and conditions of the Creative Commons Attribution (CC BY) license (<http://creativecommons.org/licenses/by/4.0/>).